

Magnetic and crystal electric field studies of two Yb³⁺-based triangular lattice antiferromagnets

S. Guchhait, R. Kolay, A. Magar, and R. Nath*

School of Physics, Indian Institute of Science Education and Research Thiruvananthapuram-695551, India

We present the low-temperature magnetic properties of two Yb³⁺-based triangular lattice compounds NaSrYb(BO₃)₂ and K₃YbSi₂O₇ via thermodynamic measurements followed by crystal electric field (CEF) calculations. Magnetization and specific heat data as well as the CEF energy levels confirm that the ground state is characterized by the low-lying Kramers' doublet of Yb³⁺ with effective spin-1/2 ($J_{\text{eff}} = 1/2$). A small Curie-Weiss temperature and scaling of magnetic isotherms corroborate very weak magnetic correlations among $J_{\text{eff}} = 1/2$ spins. The crystal field parameters are calculated using the point charge model and the CEF Hamiltonian is determined for both the compounds. The simulation using the eigenvalues of the CEF Hamiltonian reproduces the experimental susceptibility, magnetic isotherm, and magnetic specific heat data very well. The large separation between the ground state and first excited state doublets implies that the ground state is a Kramers' doublet with $J_{\text{eff}} = 1/2$ at low temperatures, endorsing the experimental findings.

I. INTRODUCTION

Quasi-two-dimensional (2D) geometrically frustrated magnets with low spin value (e.g. $S = 1/2$) have strong quantum fluctuations that melt the conventional magnetic long-range order (LRO), leading to several disordered ground states, such as, quantum spin liquid (QSL) [1]. Spin-1/2 triangular lattice antiferromagnet (TLA) is a simplest example of the geometrically frustrated lattice in 2D, was first proposed by Anderson to host resonating valence bond state, a prototype of QSL [2]. A detailed theoretical study of an isotropic Heisenberg TLA for arbitrary S -value has suggested to have a non-collinear 120° ordered state in zero-field [3, 4]. Subsequently, a series of theoretical and numerical studies on $S = 1/2$ TLA with anisotropic nearest-neighbor (NN) and next-nearest-neighbour (NNN) Heisenberg interactions have revealed numerous interesting quantum phases at the critical ratios of the exchange couplings [5–8]. Moreover, atomic disorder and vacancies are often proven to be pertinent in regards to stabilizing QSL [9–12]. Therefore, relentless efforts are being made in order to design suitable geometrically frustrated magnets which may allow to probe the intriguing ground states.

Recently, rare-earth ($4f$)-based TLAs, especially with Yb³⁺ ion, provide a new platform to investigate exotic quantum phases of matter. In contrast to transition metal oxides, the interplay between strong spin-orbit coupling (SOC) and weak crystal electric field (CEF) in $4f$ systems leads to a Kramers' doublet with an effective spin $J_{\text{eff}} = 1/2$ ground state at low temperatures [13, 14]. For instance, well-studied compounds YbMgGaO₄ and chalcogenides NaYbC₂ ($C = \text{O}, \text{S}, \text{Se}$) with $J_{\text{eff}} = 1/2$ ground state are reported to feature QSL and field-induced ordered states [15–19]. Furthermore, rare-earth-based frustrated magnets with reduced

exchange couplings are potential materials for achieving sub-Kelvin temperatures via adiabatic demagnetization refrigeration (ADR) technique [20]. Recently, a series of rare-earth-based TLAs with general formula $AA'R(\text{BO}_3)_2$ (where, $A = \text{K}, \text{Rb}, \text{Na}$; $A' = \text{Ba}, \text{Sr}$; and $R = \text{rare-earth ions}$) have demonstrated several exotic ground states and proven to be good ADR materials to reach milli-Kelvin temperatures. KBaYb(BO₃)₂ and KBaGd(BO₃)₂ are two well studied systems in this family [21, 22]. KBaYb(BO₃)₂ exhibits no magnetic LRO due to the geometrical frustration and site disorder of K⁺ and Ba²⁺ ions [21]. On the other hand, KBaGd(BO₃)₂ undergoes a magnetic LRO at around $T_N \simeq 263$ mK in zero magnetic field. Using ADR technique, one can achieve temperatures as low as ~ 122 mK and 40 mK for KBaGd(BO₃)₂ and KBaYb(BO₃)₂, respectively [22]. Interestingly, KBaGd(BO₃)₂ shows a dipolar spin-liquid phase between the antiferromagnetic order state and the paramagnetic region due to the interplay of dominant dipolar coupling and weak Heisenberg interaction [23].

Herein, we present the ground properties of two frustrated TLA compounds NaSrYb(BO₃)₂ and K₃YbSi₂O₇. NaSrYb(BO₃)₂ belongs to a family $AA'R(\text{BO}_3)_2$ and crystallizes in a monoclinic structure with space group $P2_1/m$ [24]. In the crystal structure, distorted YbO₆ octahedra are corner-shared with BO₃ triangles and put up an anisotropic 2D triangular lattice [see Fig. 1(b)] in the ab -plane. The triangular layers are well separated by the disordered Na⁺ and Sr²⁺ atoms [site (Na/Sr) mixing], as illustrated in Fig. 1(a). On the other hand, K₃YbSi₂O₇ crystallizes in a hexagonal structure with space group $P6_3/mmc$ [25]. In K₃YbSi₂O₇, regular YbO₆ octahedra are corner shared through SiO₄ tetrahedra, forming an isotropic triangular layer in the crystallographic ab -plane [see Fig. 1(d)]. These triangular planes are connected via corner-sharing of two SiO₄ units through the apical oxygen along the crystallographic c -axis and the K⁺ ions sit in-between two adjacent layers, as shown in Fig. 1(c). No conventional magnetic LRO is detected down to 0.4 K in both compounds. The crystal field calculations using

* nath@iisertvm.ac.in

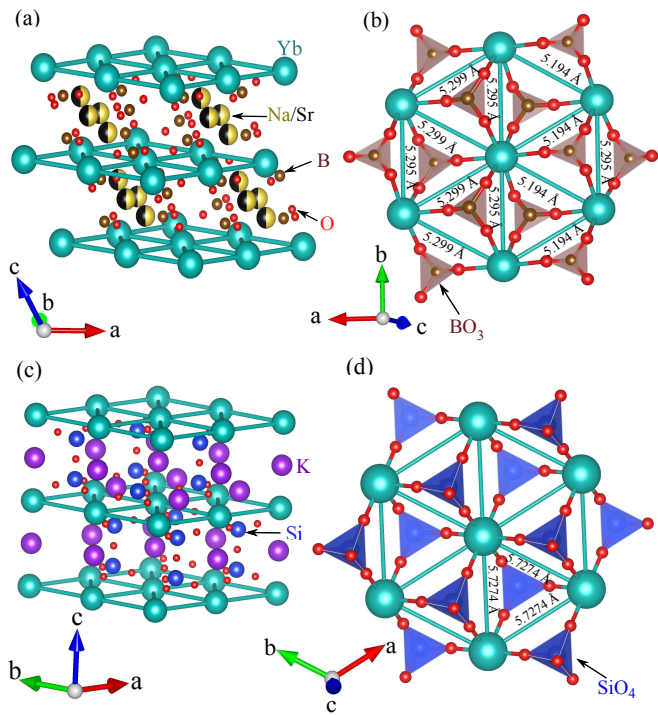


FIG. 1. (a) Crystal structure of $\text{NaSrYb}(\text{BO}_3)_2$ showing triangular layers of Yb^{3+} ions separated by Na and Sr (site mixing) atoms. (b) A section of the triangular layer showing Yb^{3+} ions linked via BO_3 units on an anisotropic triangular lattice. (c) Crystal structure of $\text{K}_3\text{YbSi}_2\text{O}_7$. (d) A section of the isotropic triangular layer formed by Yb^{3+} ions.

the point charge model give a tentative estimation of the CEF energy levels of all expected doublets for both the compounds. Finally, we simulated the magnetic susceptibility, magnetic isotherms, and specific heat using the CEF parameters and made a comparison with the experimental data.

II. METHODS

Polycrystalline sample of $\text{NaSrYb}(\text{BO}_3)_2$ was synthesized by the conventional solid-state reaction method in a platinum crucible. For its synthesis, stoichiometric mixture of Yb_2O_3 (Aldrich, 99.9%), Na_2CO_3 (Aldrich, 99.9%), SrCO_3 (Aldrich, 99.8%), and H_3BO_3 (Aldrich, 99%) was preheated at 650°C for 5 hrs to decompose the starting materials. In the next step, the mixture was ground thoroughly, pressed into pellets, and annealed at 850°C for 12 hrs. Phase purity of $\text{NaSrYb}(\text{BO}_3)_2$ was confirmed by powder x-ray diffraction (XRD) measurement at room temperature using a PANalytical x-ray diffractometer with $\text{Cu } K_\alpha$ radiation ($\lambda_{\text{avg}} \simeq 1.5418 \text{ \AA}$). Rietveld refinement of the powder XRD pattern was performed using the FULLPROF software package [26], taking the initial structural parameters of the iso-structural compound $\text{NaSrY}(\text{BO}_3)_2$ [24]. All the peaks were in-

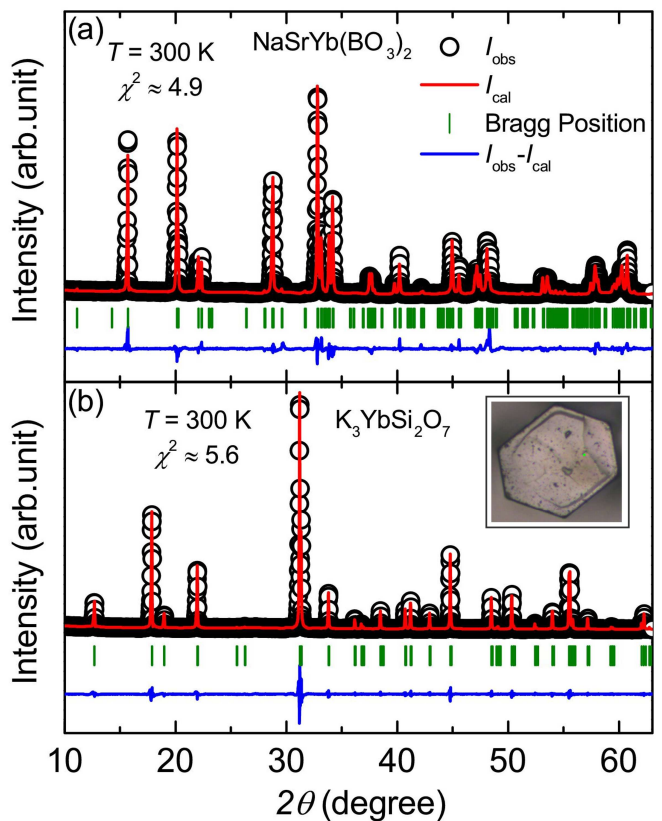


FIG. 2. Powder XRD patterns of (a) $\text{NaSrYb}(\text{BO}_3)_2$ and (b) $\text{K}_3\text{YbSi}_2\text{O}_7$ at room temperature. Red solid line represents the Rietveld fit. The black circles denote observed intensity. Green small vertical bars at the bottom show the expected Bragg peak positions and the lower blue solid line corresponds to the difference between observed and calculated intensities. χ^2 represents the goodness-of-fit of the Rietveld refinement. The inset of (b) shows the image of a single crystal of $\text{K}_3\text{YbSi}_2\text{O}_7$.

dexed properly using the monoclinic structure with space group $P2_1/m$ (No. 11) [see Fig. 2(a)]. The obtained lattice parameters and unit cell volume (V_{cell}) are $a = 9.0605(4) \text{ \AA}$, $b = 5.2958(2) \text{ \AA}$, $c = 6.4305(3) \text{ \AA}$, $\beta = 118.51(3)$, and $V_{\text{cell}} \simeq 271.12 \text{ \AA}^3$. The refined atomic coordinates of different atoms for $\text{NaSrYb}(\text{BO}_3)_2$ are listed in Table I

Single crystals of $\text{K}_3\text{YbSi}_2\text{O}_7$ were grown by the high temperature flux method. A homogeneous mixture of Yb_2O_3 (Aldrich, 99.9%) and SiO_2 (Aldrich, 99%) in a molar ratio of 1:12 (for 0.1gm of $\text{K}_3\text{YbSi}_2\text{O}_7$) and KF flux (2gm, Aldrich, 99.9%) was transferred to a platinum crucible, covered with a lid. Then, the mixture was sintered at 1000°C for 12 hrs followed by slow cooling to 800°C in a cooling rate of $0.5^\circ\text{C}/\text{min}$. Finally, the furnace was switched off and the sample was furnace cooled to room temperature. Small single crystals were manually removed, washed with distilled water, and dried in air. Single-crystal XRD on a good-quality single crystal was performed at room temper-

TABLE I. The Wyckoff positions and refined atomic coordinates for each atom of $\text{NaSrYb}(\text{BO}_3)_2$ at room temperature, obtained from the powder XRD.

Atomic sites	Wyckoff positions	x	y	z	Occ.
Yb(1)	2c	0.255(1)	0.25	0.499(2)	0.5
Na(1)	6g	0.450(2)	0.250	0.143(3)	0.241
Sr(1)	6g	0.450(2)	0.250	0.143(3)	0.259
Na(2)	6g	0.0513(2)	0.250	-0.164(3)	0.29
Sr(2)	6g	0.0513(2)	0.250	-0.164(3)	0.21
B(1)	6g	0.704(1)	0.250	-0.284(2)	0.5
B(2)	2d	0.152(9)	-0.250	0.751(2)	0.5
O(1)	6g	0.540(6)	0.250	-0.295 (7)	0.5
O(2)	6g	0.763(4)	0.024(5)	-0.207(6)	1.00
O(3)	6g	-0.027(6)	0.250	0.386(7)	0.5
O(4)	6g	0.708(4)	0.059(6)	0.239(6)	1.00

ature using a Bruker KAPPA-II diffractometer with a CCD detector and graphite monochromated Mo K_α radiation ($\lambda_{\text{avg}} \sim 0.71073 \text{ \AA}$). The data were recorded using APEX3 software and reduced with SAINT/XPREP. An empirical absorption correction was performed using the SADABS program. The crystal structure was solved by direct methods using SHELXT-2018/2 and refined by the full matrix least squares method on F^2 using SHELXL2018/3, respectively. The obtained crystal structure is Hexagonal (space group: $P6_3/mmc$) which is consistent with the previous report [25]. The details of the refined crystal structure and atomic positions are tabulated in Tables II and III, respectively. The anisotropic atomic displacement parameters are given in the supplementary material (SM) [27]. To further cross-check the phase purity, a large number of single crystals of $\text{K}_3\text{YbSi}_2\text{O}_7$ were crushed into powder and the powder XRD measurement was performed at room temperature. As shown in Fig. 2(b), the Rietveld refinement of the powder XRD pattern confirms high quality phase pure sample. The obtained lattice parameters $a = 5.7323(4) \text{ \AA}$, $c = 13.956(3) \text{ \AA}$, and $V_{\text{cell}} \simeq 397.15 \text{ \AA}^3$ agree with the single crystal XRD. Since the crystals were very small, all the measurements on this compound were done on the crushed powder sample.

Magnetization (M) as a function of temperature (T) was measured in the temperature range 0.4–380 K in different magnetic fields (H) using a superconducting quantum interference device (SQUID) magnetometer (MPMS 3, Quantum Design). For achieving temperature below 1.8 K, a ^3He insert (iHelium3) was used in SQUID. The isothermal magnetization (M vs H) was measured at different temperatures from 0 to 7 T. The temperature-dependent specific heat [$C_P(T)$] at different fields (0 T $\leq \mu_0 H \leq 9$ T) was measured on a small piece of sintered pellet in a large temperature range (0.4 K $\leq T \leq 300$ K) using the standard thermal relaxation technique in a

TABLE II. Details of the structural data of $\text{K}_3\text{YbSi}_2\text{O}_7$ obtained from the single crystal XRD.

Crystal data	
Empirical formula	$\text{K}_3\text{YbSi}_2\text{O}_7$
Formula weight (M_r)	458.52 g
Crystal system	Hexagonal
Space group	$P6_3/mmc$
a (\AA)	5.7177(6)
c (\AA)	13.9132(18)
V_{cell} (\AA^3)	393.91(10)
Z	2
Calculated crystal density ρ_{cal}	3.866 mg/mm ³
Absorption coefficient (μ)	13.758 mm ⁻¹
Crystal size	0.068 \times 0.048 \times 0.038 mm ³
Data collection	
Temperature (K)	296(2)
Radiation type	$\text{MoK}_{\alpha 1}$
Wavelength (λ)	0.71073 \AA
Diffractometer	Bruker KAPPA APEX-II CCD
θ range for data collection	2.708 $^\circ$ to 26.422 $^\circ$
Index ranges	$-7 \leq h \leq 7$, $-7 \leq k \leq 7$, $-18 \leq l \leq 18$
$F(000)$	422.0
Reflections collected	2114
Independent reflections	213 [$R_{\text{int}} = 0.0406$]
Data/restraints/parameters	213/12/19
Final R indexes, $I \geq 2\sigma(I)$	$R_1 = 0.0224$, $\omega R_2 = 0.0557$
Final R indexes, all data	$R_1 = 0.0242$, $\omega R_2 = 0.0570$
Largest difference peak/hole	1.014 / -0.487 e. \AA^{-3}
Refinement	
Refinement method	Full-matrix least-squares on F^2
Goodness-of-fit on F^2	1.128

TABLE III. The Wyckoff positions, atomic coordinates, and isotropic atomic displacement parameters (U_{iso}) for $\text{K}_3\text{YbSi}_2\text{O}_7$, obtained from the single crystal XRD. U_{iso} is defined as one-third of the trace of the orthogonal U_{ij} tensor. The error bars are from the least-square structure refinement. The occupancy is one for all the atoms.

Atomic sites	Wyckoff positions	x	y	z	U_{iso}
K(1)	4f	1/3	2/3	0.1085(2)	0.015(1)
K(2)	2b	0	0	1/4	0.02(1)
Yb(1)	2a	0	0	0	0.007 (1)
O(1)	12k	0.3642(8)	0.1821(4)	0.0841(3)	0.015(1)
O(2)	2d	2/3	1/3	1/4	0.022(2)
Si(1)	4f	2/3	1/3	0.1367(2)	0.007(1)

Physical Property Measurement System (PPMS, Quantum Design). A ^3He attachment to the PPMS was used to measure specific heat below 2 K.

The crystal electric field (CEF) calculations of both the systems were performed using the point charge model using the PyCrystalField Python package [28]. The structural parameters (lattice constants and atomic positions) used for this calculation are taken from the Rietveld refinement (I and III) of the powder XRD data. The six nearest-neighbor oxygen (O^{2-}) ligands of the YbO_6 octahedra are included in this calculation.

III. RESULTS

A. Magnetization

Temperature-dependent magnetic susceptibility $\chi[\equiv M/H]$ of $\text{NaSrYb}(\text{BO}_3)_2$ and $\text{K}_3\text{YbSi}_2\text{O}_7$ in different magnetic fields are presented in Fig. 3(a) and 4(a), respectively. In the high-temperature region, $\chi(T)$ of both compounds follows a typical Curie-Weiss (CW) behaviour. No clear signature of magnetic LRO is observed down to 0.4 K for both compounds. However, a small cusp in $d\chi/dT$ (see SM [27]) appears at around ~ 2.25 K for $\text{NaSrYb}(\text{BO}_3)_2$ in low magnetic fields, signaling the onset of magnetic LRO, arising possibly due to a tiny amount ($< 1\%$) of Yb_2O_3 impurity present in the powder sample [29]. Indeed, it is observed that the majority of the Yb^{3+} based compounds in the polycrystalline form use to have a small amount of Yb_2O_3 impurity [21, 30]. The inverse magnetic susceptibility [$1/\chi(T)$], in the high-temperature region, was well fitted by the modified CW law

$$\chi(T) = \chi_0 + \frac{C}{T - \theta_{\text{CW}}}. \quad (1)$$

Here, χ_0 is the combination of T -independent core diamagnetic (χ_{dia}) and Van-Vleck paramagnetic (χ_{VV}) susceptibilities. In the second term of Eq. (1), C is the Curie constant and θ_{CW} is the CW temperature.

The CW fit for $T \geq 90$ K yields the parameters $\chi_0^{\text{HT}} \simeq 3.1 \times 10^{-5} \text{ cm}^3/\text{mol}$, $C^{\text{HT}} \simeq 2.65 \text{ cm}^3\text{K}/\text{mol}$, and $\theta_{\text{CW}}^{\text{HT}} \simeq -78.8$ K for $\text{NaSrYb}(\text{BO}_3)_2$ [see Fig. 3(b)]. Similarly, for $\text{K}_3\text{YbSi}_2\text{O}_7$, the CW fit for $T \geq 100$ K returns $\chi_0^{\text{HT}} \simeq 1.7 \times 10^{-3} \text{ cm}^3/\text{mol}$, $C^{\text{HT}} \simeq 2.67 \text{ cm}^3\text{K}/\text{mol}$, and $\theta_{\text{CW}}^{\text{HT}} \simeq -94$ K [see Fig. 4(b)]. From the C^{HT} value, the effective moment $\mu_{\text{eff}}^{\text{HT}} [= \sqrt{\left(\frac{3k_{\text{B}}C}{N_{\text{A}}}\right)} \mu_{\text{B}}$, where N_{A} is the Avogadro's number, μ_{B} is the Bohr magneton, and k_{B} is the Boltzmann constant] is calculated to be $\sim 4.59 \mu_{\text{B}}$ and $\sim 4.62 \mu_{\text{B}}$ for $\text{NaSrYb}(\text{BO}_3)_2$ and $\text{K}_3\text{YbSi}_2\text{O}_7$, respectively. These values of $\mu_{\text{eff}}^{\text{HT}}$ are close to the expected value $\sim 4.54 \mu_{\text{B}}$ for a free Yb^{3+} ion ($J = 7/2$ and Landé g -factor $g = 1.14$) with $4f^{13}$ electronic configuration. Here, the large negative value of $\theta_{\text{CW}}^{\text{HT}}$ does not imply the presence of strong AFM interactions between

the Yb^{3+} ions. Rather, it indicates the effect of CEF excitations at high temperatures. For the Yb^{3+} ($J = 7/2$) ion, one expects the spin-orbit entangled eight-fold degenerate ground state to split into four Kramer's doublets (with quantum numbers $J_z = \pm\frac{1}{2}, \pm\frac{3}{2}, \pm\frac{5}{2},$ and $\pm\frac{7}{2}$) due to CEF interaction. At high temperatures, all the higher energy doublets get thermally populated and contribute to θ_{CW} . However, when the temperature is lowered below the energy gap between the ground state and first excited state doublets, only the lowest energy doublet is populated and contributes to the ground state properties. In the Yb^{3+} based compounds, the lowest Kramer's doublet with effective $J_{\text{eff}} = 1/2$ typically controls magnetic properties at low temperatures, while the higher-lying doublets produce a sizable Van-Vleck contribution (χ_{VV}) [31–33].

As observed in Figs. 3(b) and 4(b), $1/\chi(T)$ displays a clear slope change below about 50 K. $1/\chi(T)$ after correcting the Van-Vleck contribution [i.e. $1/(\chi - \chi_{\text{VV}})$] shows a distinct linear regime in the low-temperature side [see insets of Figs. 3(b) and 4(b)]. Here, χ_{VV} was obtained from the analysis of magnetization isotherm at $T = 0.4$ K (discussed later). A CW fit in the temperature range 2 to 20 K yields ($C^{\text{LT}} \simeq 0.84 \text{ cm}^3\text{K}/\text{mol}$ and $\theta_{\text{CW}}^{\text{LT}} \simeq -0.1$ K) for $\text{NaSrYb}(\text{BO}_3)_2$ and ($C^{\text{LT}} \simeq 0.74 \text{ cm}^3\text{K}/\text{mol}$ and $\theta_{\text{CW}}^{\text{LT}} \simeq -0.1$ K) for $\text{K}_3\text{YbSi}_2\text{O}_7$, respectively. The small negative value of $\theta_{\text{CW}}^{\text{LT}}$ suggests a very weak and dominant antiferromagnetic (AFM) interaction among the Yb^{3+} ($J_{\text{eff}} = 1/2$) ions. The obtained $C^{\text{LT}} \simeq 0.84 \text{ cm}^3\text{K}/\text{mol}$ and $0.74 \text{ cm}^3\text{K}/\text{mol}$ values are equivalent to an effective moment of $\mu_{\text{eff}}^{\text{LT}} \simeq 2.6 \mu_{\text{B}}$ and $\mu_{\text{eff}}^{\text{LT}} \simeq 2.45 \mu_{\text{B}}$ for $\text{NaSrYb}(\text{BO}_3)_2$ and $\text{K}_3\text{YbSi}_2\text{O}_7$, respectively. These values of $\mu_{\text{eff}}^{\text{LT}}$ are reminiscent of an effective spin $J_{\text{eff}} = 1/2$ ground state with an average $g_{\text{ave}} \simeq 3$ for $\text{NaSrYb}(\text{BO}_3)_2$ and $g_{\text{ave}} \simeq 2.8$ for $\text{K}_3\text{YbSi}_2\text{O}_7$. The reduced value of the effective moment or $J_{\text{eff}} = 1/2$ at low- T s can be attributed to the effect of CEF splitting and depopulation of higher energy doublets. These g -values are in close agreement with the CEF calculations (discussed later) as well as the electron spin resonance (ESR) experiments on other Yb^{3+} based systems [34, 35].

In order to have a rough estimation of CEF energy gap, we also fitted $1/\chi(T)$ by a simplified effective two-level model [36]

$$\chi(T) = \chi_0 + \frac{1}{8(T - \theta_{\text{CW}})} \times \left[\frac{\mu_{\text{eff},0}^2 + \mu_{\text{eff},1}^2 e^{-\left(\frac{\Delta^{\text{CEF}}}{k_{\text{B}}T}\right)}}{1 + e^{-\left(\frac{\Delta^{\text{CEF}}}{k_{\text{B}}T}\right)}} \right]. \quad (2)$$

Here, Δ^{CEF} is the energy gap between the ground state and the first excited CEF doublets. $\mu_{\text{eff},0}$ and $\mu_{\text{eff},1}$ are the effective moments of the ground state and the first excited CEF levels, respectively. The two-level CEF fit for $T \geq 25$ K regime yields $\chi_0^{\text{CEF}} \simeq 2.45 \times 10^{-4} \text{ cm}^3/\text{mol}$, $\mu_{\text{eff},0}^{\text{CEF}} \simeq 3.33 \mu_{\text{B}}/\text{Yb}^{3+}$, $\mu_{\text{eff},1}^{\text{CEF}} \simeq 5.53 \mu_{\text{B}}/\text{Yb}^{3+}$, $\Delta^{\text{CEF}}/k_{\text{B}} \simeq 215$ K, and $\theta_{\text{CW}}^{\text{CEF}} \simeq -10.13$ K. Similarly, in the case of $\text{K}_3\text{YbSi}_2\text{O}_7$, this fit

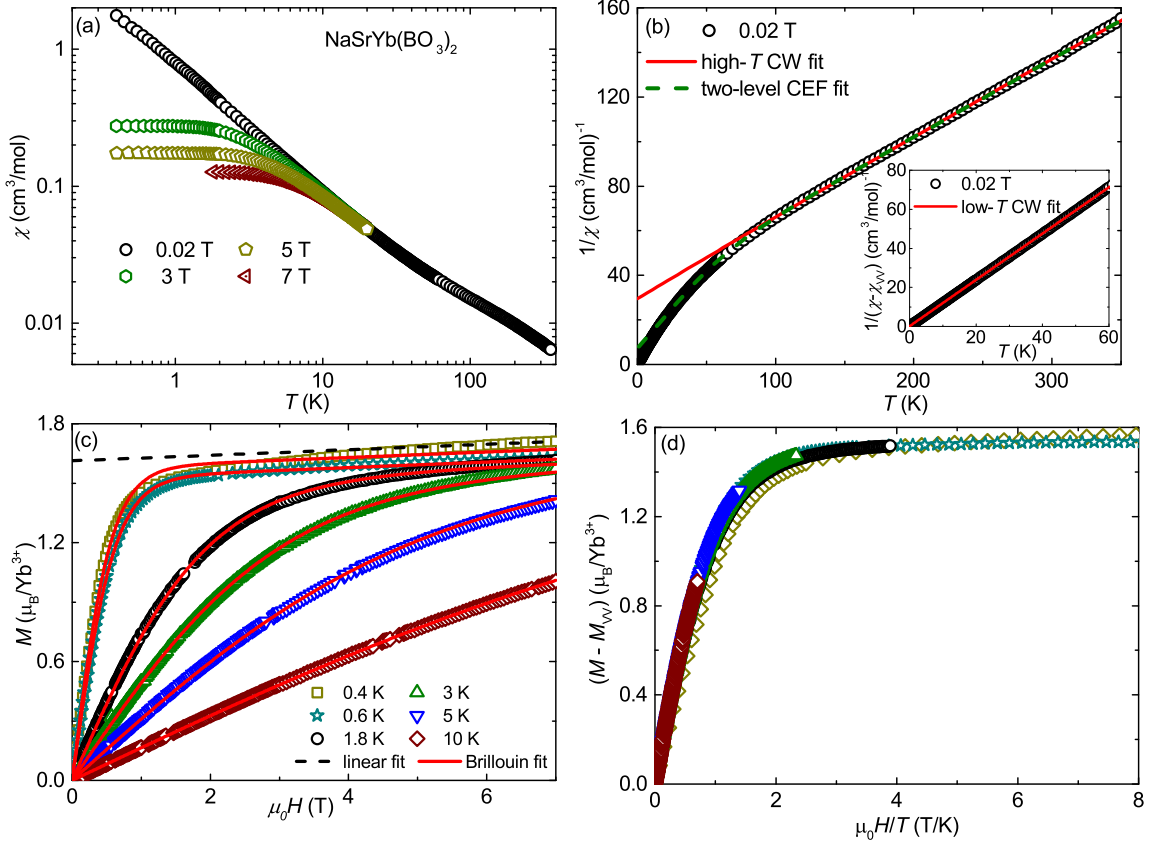


FIG. 3. (a) χ vs T of $\text{NaSrYb}(\text{BO}_3)_2$ measured in different applied magnetic fields. (b) Inverse susceptibility ($1/\chi$) vs T measured at $\mu_0 H = 0.02$ T for $\text{NaSrYb}(\text{BO}_3)_2$. The solid and dashed lines represent the high- T CW fit [Eq. (1)] and two-level CEF fit [Eq. (2)], respectively. Inset: The low-temperature $1/(\chi - \chi_{\text{VV}})$ data along with the CW fit. (c) Magnetic isotherms (M vs H) of $\text{NaSrYb}(\text{BO}_3)_2$ at different temperatures along with the Brillouin fits. The dashed line represents a linear fit to the high-field data for $T = 0.4$ K. (d) $(M - M_{\text{VV}})$ vs $\mu_0 H/T$ at different temperatures.

for $T \geq 25$ K gives $\chi_0^{\text{CEF}} \simeq 1.6 \times 10^{-3}$ cm³/mol, $\mu_{\text{eff},0}^{\text{CEF}} \simeq 3.3 \mu_{\text{B}}/\text{Yb}^{3+}$, $\mu_{\text{eff},1}^{\text{CEF}} \simeq 5.56 \mu_{\text{B}}/\text{Yb}^{3+}$, $\Delta^{\text{CEF}}/k_{\text{B}} \simeq 229$ K, and $\theta_{\text{CW}}^{\text{CEF}} \simeq -13.7$ K. These values of $\Delta^{\text{CEF}}/k_{\text{B}}$ are in the same order of magnitude as that of our CEF calculations, presented later. However, the obtained $\theta_{\text{CW}}^{\text{CEF}}$ values deviate significantly from the ones derived from the low- T $\chi(T)$ analysis [30, 37, 38]. As these parameters solely depend on the symmetry and strength of the crystal field environment, a four-level fit may be required. However, a large number of fitting parameters using a four-level fit often result unreliable values.

The magnetization isotherms $M(H)$ of $\text{NaSrYb}(\text{BO}_3)_2$ and $\text{K}_3\text{YbSi}_2\text{O}_7$ measured up to 7 T at different temperatures are shown in Figs. 3(c) and 4(c), respectively. The $M(H)$ curve at $T = 0.4$ K shows the saturation of magnetization at around $\mu_0 H_{\text{S}} \simeq 1$ T for both compounds and then increases linearly in higher fields due to the Van-Vleck paramagnetic contribution. The saturation magnetization M_{sat} and χ_{VV} of both compounds are obtained from the slope and y -intercept of a straight line fit to the data above 5 T. We obtained $\chi_{\text{VV}} \simeq 7.04 \times 10^{-3}$ cm³/mol and $M_{\text{sat}} \simeq 1.6 \mu_{\text{B}}$ for $\text{NaSrYb}(\text{BO}_3)_2$ and

$\chi_{\text{VV}} \simeq 7.66 \times 10^{-3}$ cm³/mol and $M_{\text{sat}} \simeq 1.45 \mu_{\text{B}}$ for $\text{K}_3\text{YbSi}_2\text{O}_7$, respectively. The value of M_{sat} ($M_{\text{sat}} = g_{\text{ave}} J_{\text{eff}} \mu_{\text{B}}$) corresponds to $J_{\text{eff}} = 1/2$ with an average value of $g_{\text{ave}} \simeq 3.2$ and 2.9 for $\text{NaSrYb}(\text{BO}_3)_2$ and $\text{K}_3\text{YbSi}_2\text{O}_7$, respectively. These values of g_{ave} are close to the obtained g -value for other Yb^{3+} -based compounds at low-temperatures [35, 39].

As we noticed from the $\chi(T)$ analysis that the value of $\theta_{\text{CW}}^{\text{LT}}$ is negligibly small, reflecting very weak magnetic correlations at low temperatures for both the compounds. Therefore, we tried to model the magnetic isotherms at different temperatures by the following expression [40, 41]

$$M(H) = \chi_{\text{VV}} H + N_{\text{A}} g \mu_{\text{B}} J_{\text{eff}} B J_{\text{eff}}(x), \quad (3)$$

assuming uncorrelated spins at low temperatures. Here, $B J_{\text{eff}}(x)$ is the Brillouin function and $x = g \mu_{\text{B}} J_{\text{eff}} H / (k_{\text{B}} T)$. For $J_{\text{eff}} = 1/2$, the Brillouin function reduces to $B J_{\text{eff}}(x) = \tanh(x)$ [42]. While fitting the $M(H)$ curves by Eq. (3) we fixed the value of χ_{VV} . All the curves of both compounds at low temperature are well fitted by Eq. (3), which comprehends the uncorrelated paramagnetic spins at low temperatures. In order

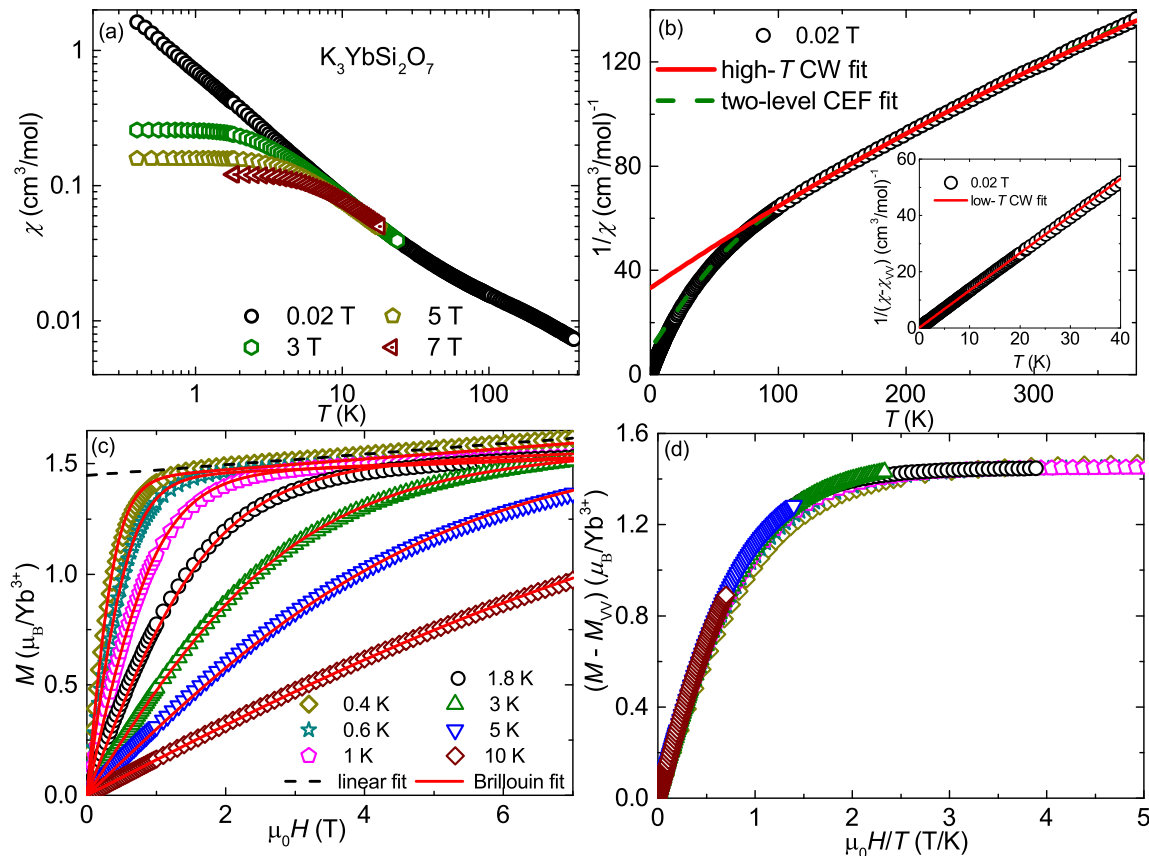


FIG. 4. (a) χ vs T of $\text{K}_3\text{YbSi}_2\text{O}_7$ measured in different applied magnetic fields. (b) Inverse susceptibility ($1/\chi$) vs T measured at $\mu_0 H = 0.02$ T for $\text{K}_3\text{YbSi}_2\text{O}_7$. The solid and dashed lines represent the high- T CW fit [Eq. (1)] and two-level CEF fit [Eq. (2)], respectively. Inset: The low-temperature $1/(\chi - \chi_{VV})$ data along with the CW fit for $\mu_0 H = 0.02$ T. (c) M vs H of $\text{K}_3\text{YbSi}_2\text{O}_7$ at different temperatures along with the Brillouin fits. The dashed line represents a linear fit to the high-field data at $T = 0.4$ K. (d) $(M - M_{VV})$ vs $\mu_0 H/T$ at different temperatures.

to further visualize this behaviour, we plotted the Van-Vleck subtracted magnetization, $M - M_{VV}$ vs $\mu_0 H/T$ at different temperatures as shown in Figs. 3(d) and 4(d). All the curves almost collapse onto a single curve, which is a clear indication of the paramagnetic nature of the spins and very weak magnetic correlation at low temperatures.

B. Specific Heat

Temperature-dependent specific heat [$C_P(T)$] of $\text{NaSrYb}(\text{BO}_3)_2$ and $\text{K}_3\text{YbSi}_2\text{O}_7$ measured down to 0.4 K in different applied fields is shown in Figs. 5(a) and 6(a), respectively. Similar to $\chi(T)$, no magnetic LRO could be detected down to 0.4 K for both the compounds. In Fig. 5(a), we observed a sharp λ -type anomaly around 2.23 K in zero field which corresponds to the magnetic ordering due to a small fraction (see SM [27]) of extrinsic Yb_2O_3 phase in $\text{NaSrYb}(\text{BO}_3)_2$. In a magnetic insulator, the total specific heat $C_P(T)$ is the sum of phonon/lattice contribution [$C_{\text{ph}}(T)$], which dominates

in the high-temperature region and magnetic specific heat [$C_{\text{mag}}(T)$], which dominates in the low-temperature region. In order to extract $C_{\text{mag}}(T)$, we subtracted $C_{\text{ph}}(T)$ from $C_P(T)$. To quantify $C_{\text{ph}}(T)$, the zero-field $C_P(T)$ was fitted by a polynomial ($= aT^3 + bT^5 + cT^7$) function for $T \geq 10$ K [43]. The obtained values of fitting parameters (a , b , and c) are given in SM [27]. The fit was extrapolated down to 0.4 K and then subtracted from the total specific heat. The obtained $C_{\text{mag}}(T)$ data at various fields are plotted in Figs. 5(b) and 6(b) for $\text{NaSrYb}(\text{BO}_3)_2$ and $\text{K}_3\text{YbSi}_2\text{O}_7$, respectively. The magnetic entropy [$S_{\text{mag}}(T)$] released at different fields are estimated by integrating C_{mag}/T over temperature. The estimated $S_{\text{mag}}(T)$ at different fields are presented in Figs. 5(c) and 6(c) for $\text{NaSrYb}(\text{BO}_3)_2$ and $\text{K}_3\text{YbSi}_2\text{O}_7$, respectively. For both the compounds, $S_{\text{mag}}(T)$ attains a value ~ 5.6 $\text{J}\cdot\text{mol}^{-1}\cdot\text{K}^{-1}$ at around 30 K in high fields, which is close to the expected value for a two-level system ($R \ln 2 = 5.76$ $\text{J}\cdot\text{mol}^{-1}\cdot\text{K}^{-1}$, where, R is the universal gas constant). This confirms a Kramers' doublet with $J_{\text{eff}} = 1/2$ ground state at low temperatures for both the compounds.

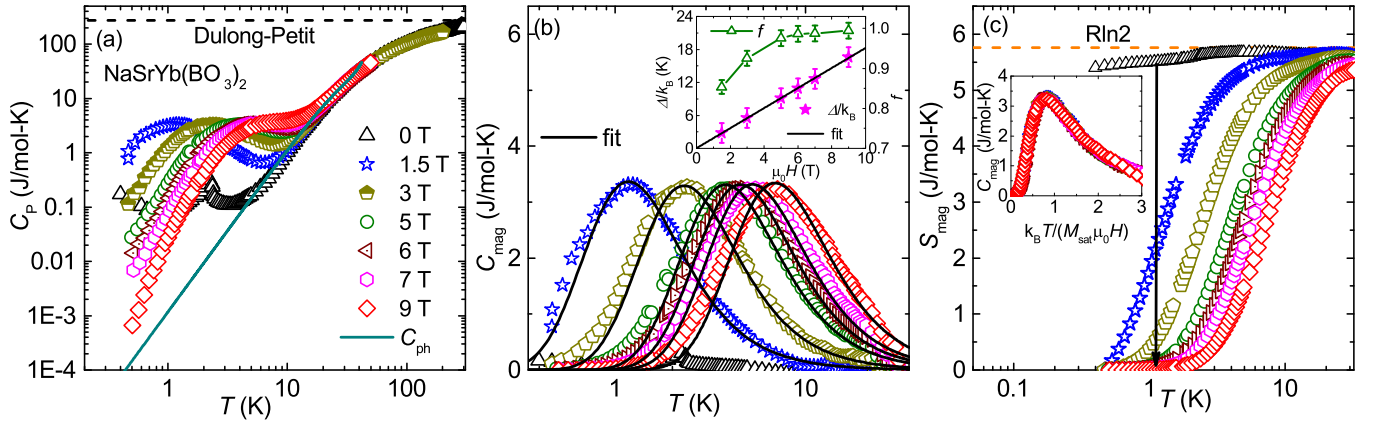


FIG. 5. (a) Variation of C_p with temperature for $\text{NaSrYb}(\text{BO}_3)_2$ measured in different applied magnetic fields. The dark cyan solid line represents the phonon specific heat (C_{ph}) obtained by the polynomial fit. The horizontal dashed line indicates the expected Dulong-Petit value for this compound. (b) C_{mag} vs T at different magnetic fields along with two-level Schottky fits. Inset: Δ/k_B vs $\mu_0 H$ (left y -axes) and f vs $\mu_0 H$ (right y -axes). The solid line is the linear fit to $\Delta/k_B(H)$. (c) The magnetic entropy change, S_{mag} vs T at different applied fields. The zero-field entropy is scaled to match $R \ln 2$ and the vertically downward arrow indicates the entropy change between 0 and 9 T. Inset: Scaling C_{mag} vs $k_B T / (M_{\text{sat}} \mu_0 H)$ plots in different magnetic fields.

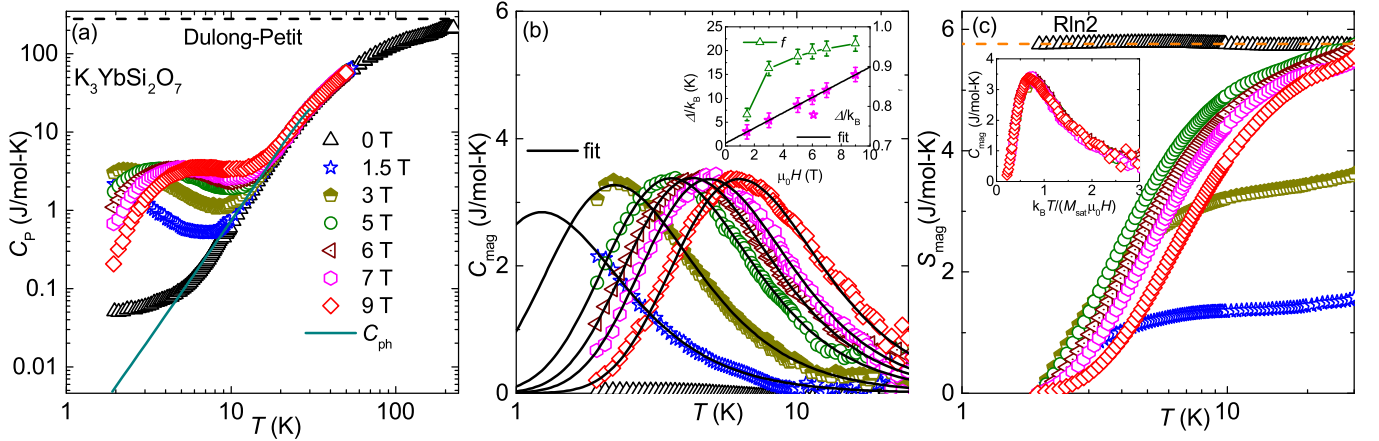


FIG. 6. (a) Variation of C_p with temperature for $\text{K}_3\text{YbSi}_2\text{O}_7$ measured in different applied magnetic fields. The dark cyan solid line represents the phonon specific heat (C_{ph}) obtained by the polynomial fit. The horizontal dashed line indicates the expected Dulong-Petit value of this compound. (b) C_{mag} vs T at different magnetic fields along with two-level Schottky fits. Inset: Δ/k_B vs $\mu_0 H$ (left y -axes) and f vs $\mu_0 H$ (right y -axes). The solid line is the linear fit of $\Delta/k_B(H)$. (c) The magnetic entropy change, S_{mag} vs T at different applied fields. The zero-field entropy is scaled to match $R \ln 2$. Inset: Scaling C_{mag} vs $k_B T / (M_{\text{sat}} \mu_0 H)$ plots in different magnetic fields.

In zero-field, $C_p(T)$ shows an upturn towards lower temperatures, implying the development of AFM correlation and the entropy accumulation associated with the lowest Kramers' doublet of Yb^{3+} . In zero-field, the entire entropy of $R \ln 2$ associated with the lowest Kramers' doublet could not be recovered as we did not have data below 0.4 K. Therefore, the zero-field entropy in Figs. 5(c) and 6(c) is vertically shifted to match with the high-field data. The ground-state doublet is split by the applied field into $J_z = +1/2$ and $J_z = -1/2$ levels, causing a Schottky anomaly (broad maximum in specific heat), which shifts toward higher temperatures with increasing field. To estimate the Schottky contribution, $C_{\text{mag}}(T)$

was fitted using the two-level Schottky function

$$C_{\text{Sch}}(T, H) = fR \left(\frac{\Delta}{k_B T} \right)^2 \frac{e^{\left(\frac{\Delta}{k_B T} \right)}}{\left[e^{\left(\frac{\Delta}{k_B T} \right)} + 1 \right]^2}. \quad (4)$$

Here, f is the molar fraction of free spins and Δ/k_B is the crystal field energy gap between the Zeeman levels of split ground state doublet. As shown in Figs. 5(b) and 6(b), $C_{\text{mag}}(T)$ data of both compounds are well fitted by Eq. (4). The estimated fitting parameters, f and Δ/k_B are plotted as a function of applied field in the inset of Figs. 5(b) and 6(b) for $\text{NaSrYb}(\text{BO}_3)_2$ and

$\text{K}_3\text{YbSi}_2\text{O}_7$, respectively. The value of f increases with H and almost saturates to 1 in higher fields. This indicates that the applied field causes splitting of the energy levels and excites the free Yb^{3+} spins to higher energy states. Below the saturation field, a small fraction of spins are correlated, which decreases with increasing field. Above the saturation field all the free spins are excited and S_{mag} saturates to a value $Rln2$. Δ/k_B increases linearly with H and a straight line fit yields a very small zero-field energy gap $\Delta/k_B(0) \simeq 0.035$ K and ~ 0.5 K, respectively. The small value of $\Delta/k_B(0)$ suggest the presence of a weak intrinsic field in these systems [11]. Using the value of $\Delta/k_B \simeq 16.13$ K at 9 T, g ($= \Delta/\mu_B H$) is calculated to be ~ 2.75 for $\text{NaSrYb}(\text{BO}_3)_2$. Similarly, using $\Delta/k_B \simeq 14.98$ K at 9 T, we obtained $g \simeq 2.5$. These g values for both the compounds are consistent with other Yb^{3+} based systems [35].

A scaling plot of C_{mag} vs $k_B T/M_{\text{sat}}\mu_0 H$ for both the compounds are shown in the inset of Figs. 5(c) and 6(c). The scaling of all the fields for $\mu_0 H \geq 0.5$ T collapse in to a single curve which indicates that the interaction strength between the Yb^{3+} ions is very small, which is consistent with very small value of $\theta_{\text{CW}}^{\text{LT}}$. Further, the Kramers' doublets can be characterized by a dimensionless quantity $R = \left(\frac{\mu_{\text{eff}}}{M_{\text{sat}}}\right)^2 = 3$. Using the experimental values of $\mu_{\text{eff}}^{\text{LT}}$ and M_{sat} , the value of R is calculated to be $R \simeq 3.04$ and 2.9 for $\text{NaSrYb}(\text{BO}_3)_2$ and $\text{K}_3\text{YbSi}_2\text{O}_7$, respectively, which are close to the theoretical expected value for a $J_{\text{eff}} = 1/2$ system [31, 44].

C. CEF analysis

To understand the single-ion effects on the ground state properties and to estimate the CEF energy level scheme of the doublets, we performed the CEF calculation using the point charge approximation method [45]. Yb^{3+} has a $4f^{13}$ electronic configuration ($L = 3$, $S = 1/2$, and $J = 7/2$). This spin-orbit coupled eight-fold ($2J+1$) degenerate states further split into four Kramer's doublets with quantum numbers $J_z = \pm\frac{1}{2}$, $\pm\frac{3}{2}$, $\pm\frac{5}{2}$, and $\pm\frac{7}{2}$. According to the Stevens convention, the CEF Hamiltonian can be written as [46]

$$\mathcal{H}_{\text{CEF}} = \sum_{l,m} B_l^m \hat{O}_l^m. \quad (5)$$

Here, \hat{O}_l^m are the Stevens operators, which are related to the angular momentum operators [46, 47]. B_l^m are the multiplicative factors, called CEF parameters, which are related to the electronic structure of the rare-earth materials. Here, the even integer l varies from 0 to 6 for f electrons and the integer m ranges from $-l$ to l . In $\text{NaSrYb}(\text{BO}_3)_2$, distorted YbO_6 octahedra generates a low-symmetry CEF environment (C_{2h}) around the Yb^{3+} ions. On the other hand, the regular YbO_6 octahedra of $\text{K}_3\text{YbSi}_2\text{O}_7$ produces a symmetric CEF environment (D_{2h}) around the Yb^{3+} ions.

TABLE IV. Calculated CEF parameters for $\text{NaSrYb}(\text{BO}_3)_2$ and $\text{K}_3\text{YbSi}_2\text{O}_7$.

NaSrYb(BO ₃) ₂		K ₃ YbSi ₂ O ₇	
B_l^m (meV)	Values	B_l^m (meV)	Values
B_2^0	-1.233×10^{-1}	B_2^0	9.252×10^{-1}
B_2^1	-1.789	B_2^1	1×10^{-8}
B_2^2	1.6176	B_4^0	3.454×10^{-1}
B_4^0	-4.032×10^{-2}	B_4^3	-9.055×10^{-1}
B_4^1	5.369×10^{-3}	B_6^0	1.595×10^{-4}
B_4^2	2.482×10^{-3}	B_6^3	3.768×10^{-3}
B_4^3	-2.675×10^{-2}	B_6^6	1.782×10^{-3}
B_4^4	2.026×10^{-1}		
B_6^0	5.911×10^{-5}		
B_6^1	-4.117×10^{-4}		
B_6^2	3.352×10^{-4}		
B_6^3	-3.782×10^{-4}		
B_6^4	1.909×10^{-3}		
B_6^5	2.795×10^{-4}		
B_6^6	-6.849×10^{-4}		

The allowed CEF parameters calculated for these two compounds using the point charge model are tabulated in Table IV. These parameters determine the actual CEF Hamiltonian of these compounds [Eq. (5)]. Next, we diagonalized the Hamiltonian and obtained the CEF energy eigenvalues of these compounds. The obtained energy eigenvalues are 0, 23.13, 41.2, and 86.2 meV, corresponding to four Kramer's doublets of $\text{NaSrYb}(\text{BO}_3)_2$, as shown in Fig. 7. Similarly, the obtained CEF energy eigenvalues of $\text{K}_3\text{YbSi}_2\text{O}_7$ are 0, 32.2, 47.6, and 100.2 meV. From the CEF Hamiltonian [Eq. (5)], the wave functions corresponding to all the Kramer's doublets can be written as

$$|\psi_k, \pm\rangle = \sum_{m_J = -\frac{7}{2}}^{m_J = \frac{7}{2}} C_{m_J}^{k, \pm} \left| J = \frac{7}{2}, m_J \right\rangle. \quad (6)$$

Here, $C_{m_J}^{k, \pm}$ are the weighted coefficients of the eigenstates and $k = 0, 1, 2$, and 3 represent the CEF energy levels. The full list of energy eigenvalues and the corresponding coefficients ($C_{m_J}^{k, \pm}$) of different eigenstates for $\text{NaSrYb}(\text{BO}_3)_2$ are listed in Table V. The wave function of the ground state doublet (lowest energy doublet) of $\text{NaSrYb}(\text{BO}_3)_2$ is obtained to be

$$\begin{aligned} |\psi_0, \pm\rangle = & \pm 0.734 \left| \pm \frac{1}{2} \right\rangle - 0.0038 \left| \mp \frac{1}{2} \right\rangle \pm 0.027 \left| \pm \frac{3}{2} \right\rangle \\ & \mp 0.0472 \left| \mp \frac{3}{2} \right\rangle \mp 0.103 \left| \pm \frac{5}{2} \right\rangle \pm 0.058 \left| \mp \frac{5}{2} \right\rangle \mp 0.669 \left| \mp \frac{7}{2} \right\rangle. \end{aligned} \quad (7)$$

Similarly, the wave function of lowest-energy doublet of

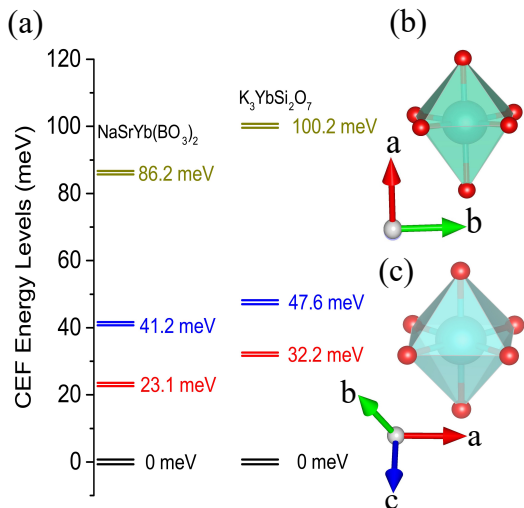


FIG. 7. (a) Schematic representation of CEF energy levels of NaSrYb(BO₃)₂ (0, 23.1, 41.2, and 86.2 meV) and K₃YbSi₂O₇ (0, 32.2, 47.6, and 100.2 meV) obtained from the point charge calculations. (b) Distorted YbO₆ octahedra of NaSrYb(BO₃)₂ (c) Regular YbO₆ octahedra of K₃YbSi₂O₇ formed by Yb³⁺ and O²⁻ ions that generate CEF.

K₃YbSi₂O₇ is

$$|\psi_0, \pm\rangle = 0.573 \left| \pm \frac{1}{2} \right\rangle \pm 0.784 \left| \pm \frac{5}{2} \right\rangle \pm 0.238 \left| \pm \frac{7}{2} \right\rangle. \quad (8)$$

The complete list of energy eigenvalues and the corresponding coefficients ($C_{m,J}^{k,\pm}$) of all the doublets of K₃YbSi₂O₇ are tabulated in Table VI.

We have also calculated the g -tensors from the point charge CEF calculations. For NaSrYb(BO₃)₂, we got $g_{\perp} \simeq 2.50$ and $g_z \simeq 2.9$, yielding an average g -value of $g_{\text{ave}} = (2g_{\perp} + g_z)/3 \simeq 2.63$, which is close to the value obtained from the low-temperature magnetization analysis. Similarly, the calculated g -components for K₃YbSi₂O₇ are $g_{\perp} \simeq 2.63$ and $g_z \simeq 2.68$. The average value $g_{\text{ave}} = (2g_{\perp} + g_z)/3 \simeq 2.65$ is also in close agreement with the one obtained from the low-temperature magnetization analysis. Further, almost equal values g_{\perp} and g_z indicates a negligibly small magnetic anisotropy in these compounds.

Using eigenvalues of the CEF Hamiltonian, we have calculated the crystal field magnetic susceptibility (χ_{CEF} vs T) and magnetization isotherms (M_{CEF} vs H). The magnetization is estimated by calculating the expectation value of total angular momentum (\hat{J}) with components J_x , J_y , and J_z as

$$M_{\text{CEF}}(T, H) = \frac{N_A g \mu_B}{Z} \times \sum_k e^{-\frac{E_k(H)}{k_B T}} \langle \psi_k(H) | \hat{J}_{\alpha} = x, y, z | \psi_k(H) \rangle. \quad (9)$$

Here, $Z = \sum_k e^{-E_k(H)/k_B T}$ is the partition function, where the summation is taken over all the energy states.

χ_{CEF} can be calculated by taking the first derivative of $M(T, H)$ with respect to H . Figures 8(a) and (b) present the calculated χ_{CEF} and M_{CEF} for NaSrYb(BO₃)₂ along with the experimental data. In both cases, we added the Van-Vleck contribution (χ_{VV} and M_{VV}) to the calculated data and our simulation reproduces the experimental data very well. Similarly, we have also calculated the χ_{CEF} and M_{CEF} for K₃YbSi₂O₇, which are in very good agreement with the experimental data [see Figs. 9(a) and (b)].

The crystal field specific heat (C_{CEF}) as a function of temperature in different fields are calculated taking into account the contributions from all the Zeeman split CEF levels. For an N level system, C_{CEF} can be written as

$$C_{\text{CEF}}(T, H) = \frac{R}{(Zk_B T)^2} \times \sum_{n>m}^N [E_n(H) - E_m(H)]^2 e^{-\frac{|E_n(H) + E_m(H)|}{k_B T}}. \quad (10)$$

Here, E_n and E_m are the energy of the n^{th} and m^{th} CEF levels, respectively. The calculated C_{CEF} reproduce the broad maximum in experimental C_{mag} of both compounds very well in the low-temperature regime [see Figs. 8(c) and 9(c)]. As we have observed in Figs. 5(b) and 6(b), the broad maximum in $C_{\text{mag}}(T)$ (in the presence of an applied field) can also be reproduced well by a simple two-level model, reflecting that only the Zeeman split ground state doublet contributes at low temperatures and the effect from the excited CEF levels is negligible. This is also evident from Fig. 7 that the ground state of both the compounds is well separated from the first excited state (~ 265 K and 370 K for NaSrYb(BO₃)₂ and K₃YbSi₂O₇, respectively), comprehending our assessment of $J_{\text{eff}} = 1/2$ ground state.

IV. DISCUSSION

The low-temperature properties of NaSrYb(BO₃)₂ and K₃YbSi₂O₇ are described by $J_{\text{eff}} = 1/2$ ground state with Kramers' doublet, which is typical for the Yb³⁺ based systems [48]. The obtained values of $\theta_{\text{CW}}^{\text{LT}}$ for both the systems are very small, implying negligible magnetic interaction among the Yb³⁺ ions. The energy scale of the dipolar interaction between the nearest-neighbor moments is estimated to be $D = \frac{2\mu_0\mu_{\text{sat}}^2}{4\pi d^3} \simeq 0.022$ K for NaSrYb(BO₃)₂ and ~ 0.014 K for K₃YbSi₂O₇ [31, 49]. Here, d is the distance between NN Yb³⁺ ions, μ_0 is the permeability of free space. From the value of $\theta_{\text{CW}}^{\text{LT}}$ one can estimate the average value of nearest-neighbour exchange coupling (J_{NN}/k_B) as $\theta_{\text{CW}}^{\text{LT}} = -zJ_{\text{eff}}(J_{\text{eff}} + 1)J_{\text{NN}}/3k_B$ [50]. Taking the magnetic coordination number $z = 6$ for a triangular lattice and using the experimental value of $\theta_{\text{CW}}^{\text{LT}}$ we got $J_{\text{NN}} \simeq 0.06$ K for both the compounds. This value of J_{NN} is slightly larger than the dipolar interaction, the effect of which can only be

TABLE V. Energy eigenvalues and the coefficients ($C_{m_J}^{k,\pm}$) corresponding to different eigenstates of the CEF Hamiltonian for $\text{NaSrYb}(\text{BO}_3)_2$.

E (meV)	$ \pm \frac{7}{2}\rangle$	$ \pm \frac{5}{2}\rangle$	$ \pm \frac{3}{2}\rangle$	$ \pm \frac{1}{2}\rangle$	$ \frac{1}{2}\rangle$	$ \frac{3}{2}\rangle$	$ \frac{5}{2}\rangle$	$ \frac{7}{2}\rangle$
0.00	-0.6697	0.0576	-0.0472	-0.0038	0.7336	0.0276	-0.103	0
0.00	0	0.103	0.0276	-0.7336	-0.0038	0.0472	0.0576	0.6697
23.13	0.216	-0.202	0.001	-0.469	0.18	0.618	-0.038	-0.52
23.13	-0.52	0.038	0.618	-0.18	-0.469	-0.001	-0.202	-0.216
41.2	-0.182	0.499	-0.493	-0.328	-0.19	-0.31	0.247	-0.418
41.2	-0.418	-0.247	-0.31	-0.19	-0.328	0.493	0.499	0.182
86.2	0	0.556	-0.224	0.199	-0.155	0.477	-0.57	0.16
86.2	0.16	0.57	0.477	0.155	0.199	0.224	0.556	0

TABLE VI. Energy eigenvalues and the coefficients ($C_{m_J}^{k,\pm}$) corresponding to different eigenstates of the CEF Hamiltonian for $\text{K}_3\text{YbSi}_2\text{O}_7$.

E (meV)	$ \pm \frac{7}{2}\rangle$	$ \pm \frac{5}{2}\rangle$	$ \pm \frac{3}{2}\rangle$	$ \pm \frac{1}{2}\rangle$	$ \frac{1}{2}\rangle$	$ \frac{3}{2}\rangle$	$ \frac{5}{2}\rangle$	$ \frac{7}{2}\rangle$
0.00	0	-0.784	0	0	0.573	0	0	0.238
0.00	-0.238	0	0	0.573	0	0	0.784	0
32.2	0	0	0.999	0	0	0.052	0	0
32.2	0	0	0.052	0	0	-0.999	0	0
47.6	0.541	0	0	-0.592	0	0	0.597	0
47.6	0	-0.597	0	0	-0.592	0	0	-0.541
100.2	0	0.169	0	0	0.566	0	0	-0.807
100.2	-0.807	0	0	-0.566	0	0	0.169	0

observed at extremely low temperatures ($T < 0.1$ K). Interestingly, there is a site mixing of Na^+ and Sr^{2+} ions that may provide randomness in the exchange interactions, an essential ingredient for suppressing magnetic LRO and holds propensity to entertain QSL [10].

For both compounds, the ground-state doublet wave function has substantial weightages coming from $|\pm \frac{1}{2}\rangle$, $|\pm \frac{5}{2}\rangle$, and $|\pm \frac{7}{2}\rangle$ states. While a large coefficient of $|\pm \frac{1}{2}\rangle$ implies significant quantum effect, the classical behaviour of the ground state is also equally probable since $|\pm \frac{5}{2}\rangle$ and $|\pm \frac{7}{2}\rangle$ also contribute to the ground state wavefunctions. Similar physics is also reported in other rare-earth based systems [28].

Moreover, because of their frustrated geometry, weak exchange couplings, and chemical stability in ultra-high vacuum and high temperatures, these compounds are potential materials for ADR technique to achieve temperatures as low as few milli-Kelvins [20, 21]. This is indeed evident from the entropy change between 0 and 9 T in Fig. 5(c).

V. SUMMARY

In summary, we present magnetization, specific heat, and crystal field analysis of Yb-based triangular lattice

compounds $\text{NaSrYb}(\text{BO}_3)_2$ and $\text{K}_3\text{YbSi}_2\text{O}_7$. There is no evidence of magnetic LRO or spin freezing down to 0.4 K for both the compounds. Thermodynamic data suggest $J_{\text{eff}} = 1/2$ ground state due to Kramers' doublet, which is also reflected from point-charge CEF calculations. Due to very weak interaction among the $J_{\text{eff}} = 1/2$ spins, the bulk magnetic properties are predicted by the point charge CEF model calculations only (without a magnetic term) which qualitatively reproduce our experimental results. The inelastic neutron scattering (INS) and Raman scattering experiments would be useful in order to confirm the proposed CEF scheme. Furthermore, these two materials seem to be a good alternative to hydrated paramagnetic salts for ADR applications to attain sub-Kelvin temperatures.

VI. ACKNOWLEDGMENTS

We would like to acknowledge SERB, India, for financial support bearing sanction Grant No. CRG/2019/000960. SG was supported by the Prime Minister's Research Fellowship (PMRF) scheme, Government of India.

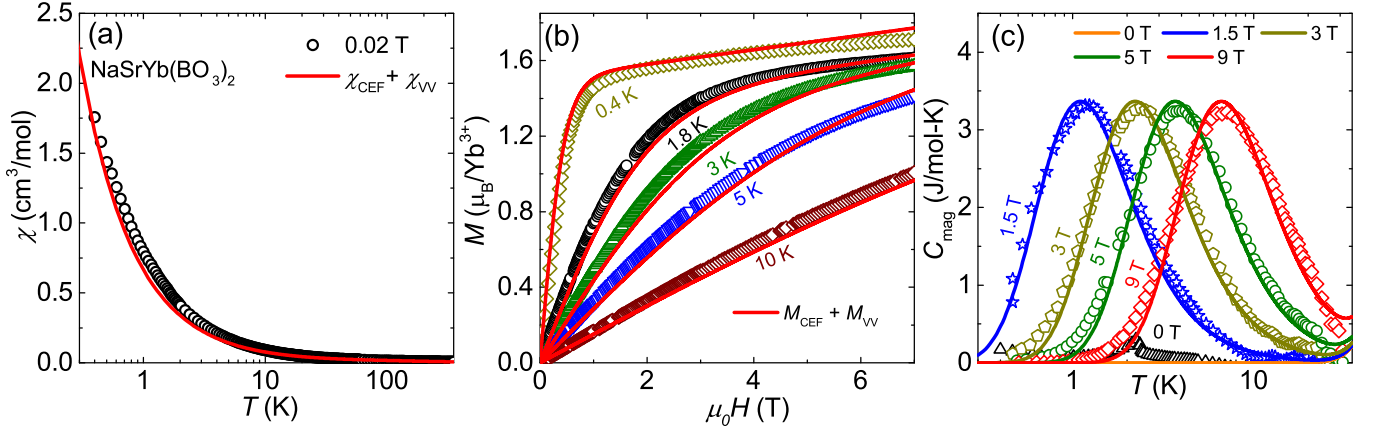


FIG. 8. (a) Experimental $\chi(T)$ of $\text{NaSrYb}(\text{BO}_3)_2$ is compared with the calculated susceptibility using the CEF model. (b) Simulated isothermal magnetization at different temperatures using the CEF model and compared with the experimental data. (c) Calculation of CEF specific heat (C_{CEF} vs T) in different magnetic fields compared with the experimental C_{mag} .

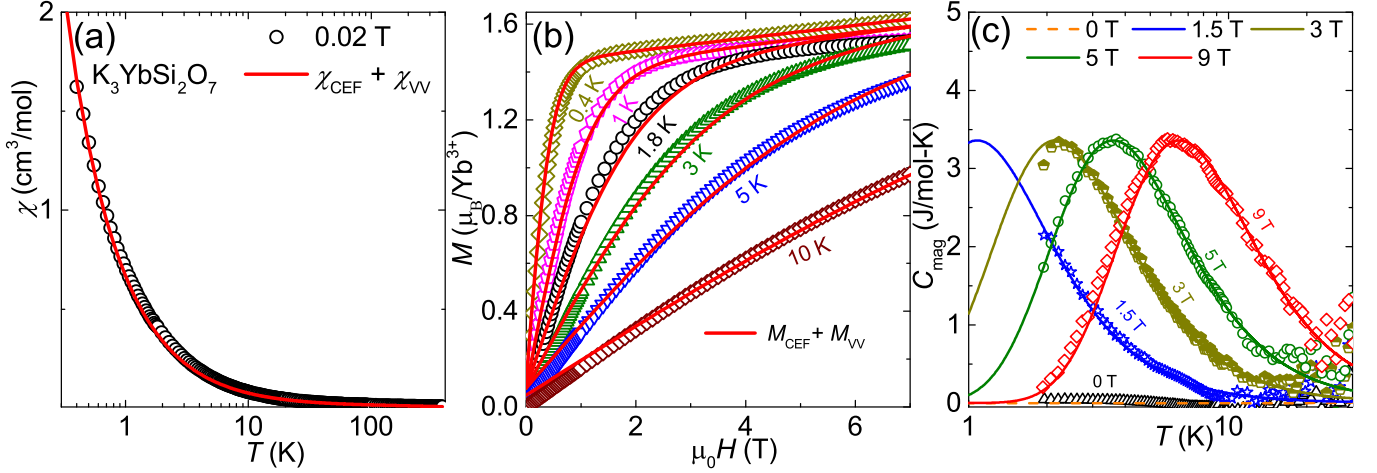


FIG. 9. (a) $\chi(T)$ of $\text{K}_3\text{YbSi}_2\text{O}_7$ is compared with the calculated susceptibility data using the CEF model. (b) Simulated isothermal magnetization at different temperatures using the CEF model and compared with the experimental data. (c) Calculation of CEF specific heat (C_{CEF} vs T) in different magnetic fields compared with the experimental C_{mag} .

-
- [1] L. Savary and L. Balents, Quantum spin liquids: a review, *Rep. Prog. Phys.* **80**, 016502 (2016); L. Balents, Spin liquids in frustrated magnets, *Nature* **464**, 199 (2010).
- [2] P. Anderson, Resonating valence bonds: A new kind of insulator?, *Mater. Res. Bull.* **8**, 153 (1973).
- [3] R. R. P. Singh and D. A. Huse, Three-sublattice order in triangular- and Kagomé-lattice spin-half antiferromagnets, *Phys. Rev. Lett.* **68**, 1766 (1992).
- [4] L. Capriotti, A. E. Trumper, and S. Sorella, Long-Range Néel Order in the Triangular Heisenberg Model, *Phys. Rev. Lett.* **82**, 3899 (1999).
- [5] Z. Zhu, P. A. Maksimov, S. R. White, and A. L. Chernyshev, Topography of Spin Liquids on a Triangular Lattice, *Phys. Rev. Lett.* **120**, 207203 (2018).
- [6] M. Drescher, L. Vanderstraeten, R. Moessner, and F. Pollmann, Dynamical signatures of symmetry-broken and liquid phases in an $S = \frac{1}{2}$ Heisenberg antiferromagnet on the triangular lattice, *Phys. Rev. B* **108**, L220401 (2023).
- [7] Z. Zhu and S. R. White, Spin liquid phase of the $S = \frac{1}{2}$ $J_1 - J_2$ Heisenberg model on the triangular lattice, *Phys. Rev. B* **92**, 041105 (2015).
- [8] W.-J. Hu, S.-S. Gong, W. Zhu, and D. N. Sheng, Competing spin-liquid states in the spin- $\frac{1}{2}$ Heisenberg model on the triangular lattice, *Phys. Rev. B* **92**, 140403 (2015).
- [9] I. Kimchi, A. Nahum, and T. Senthil, Valence Bonds in Random Quantum Magnets: Theory and Application to YbMgGaO_4 , *Phys. Rev. X* **8**, 031028 (2018).
- [10] Y. Li, D. Adroja, R. I. Bewley, D. Vonshen, A. A. Tsirlin, P. Gegenwart, and Q. Zhang, Crystalline Electric-

- Field Randomness in the Triangular Lattice Spin-Liquid YbMgGaO_4 , *Phys. Rev. Lett.* **118**, 107202 (2017).
- [11] S. Kundu, A. Hossain, P. K. S., R. Das, M. Baenitz, P. J. Baker, J.-C. Orain, D. C. Joshi, R. Mathieu, P. Mahadevan, S. Pujari, S. Bhattacharjee, A. V. Mahajan, and D. D. Sarma, Signatures of a Spin- $\frac{1}{2}$ Cooperative Paramagnet in the Diluted Triangular Lattice of Y_2CuTiO_6 , *Phys. Rev. Lett.* **125**, 117206 (2020).
- [12] Z. Zhu, P. A. Maksimov, S. R. White, and A. L. Chernyshev, Disorder-Induced Mimicry of a Spin Liquid in YbMgGaO_4 , *Phys. Rev. Lett.* **119**, 157201 (2017).
- [13] K. Somesh, Y. Furukawa, G. Simutis, F. Bert, M. Prinz-Zwick, N. Büttgen, A. Zorko, A. A. Tsirlin, P. Mendels, and R. Nath, Universal fluctuating regime in triangular chromate antiferromagnets, *Phys. Rev. B* **104**, 104422 (2021).
- [14] S. Lal, S. J. Sebastian, S. S. Islam, M. P. Saravanan, M. Uhlarz, Y. Skourski, and R. Nath, Double magnetic transitions and exotic field-induced phase in the triangular lattice antiferromagnets $\text{Sr}_3\text{Co}(\text{Nb}, \text{Ta})_2\text{O}_9$, *Phys. Rev. B* **108**, 014429 (2023).
- [15] Y. Li, D. Adroja, P. K. Biswas, P. J. Baker, Q. Zhang, J. Liu, A. A. Tsirlin, P. Gegenwart, and Q. Zhang, Muon Spin Relaxation Evidence for the U(1) Quantum Spin-Liquid Ground State in the Triangular Antiferromagnet YbMgGaO_4 , *Phys. Rev. Lett.* **117**, 097201 (2016).
- [16] P.-L. Dai, G. Zhang, Y. Xie, C. Duan, Y. Gao, Z. Zhu, E. Feng, Z. Tao, C.-L. Huang, H. Cao, A. Podlesnyak, G. E. Granroth, M. S. Everett, J. C. Neuefeind, D. Vonshen, S. Wang, G. Tan, E. Morosan, X. Wang, H.-Q. Lin, L. Shu, G. Chen, Y. Guo, X. Lu, and P. Dai, Spinon Fermi Surface Spin Liquid in a Triangular Lattice Antiferromagnet NaYbSe_2 , *Phys. Rev. X* **11**, 021044 (2021).
- [17] Y. Li, D. Adroja, D. Vonshen, R. I. Bewley, Q. Zhang, A. A. Tsirlin, and P. Gegenwart, Nearest-neighbour resonating valence bonds in YbMgGaO_4 , *Nat. Commun.* **8**, 15814 (2017).
- [18] R. Sarkar, P. Schlender, V. Grinenko, E. Haeussler, P. J. Baker, T. Doert, and H.-H. Klauss, Quantum spin liquid ground state in the disorder free triangular lattice NaYbS_2 , *Phys. Rev. B* **100**, 241116 (2019).
- [19] A. O. Scheie, Y. Kamiya, H. Zhang, S. Lee, A. J. Woods, M. O. Ajeesh, M. G. Gonzalez, B. Bernu, J. W. Villanova, J. Xing, Q. Huang, Q. Zhang, J. Ma, E. S. Choi, D. M. Pajerowski, H. Zhou, A. S. Sefat, S. Okamoto, T. Berlijn, L. Messio, R. Movshovich, C. D. Batista, and D. A. Tennant, Nonlinear magnons and exchange Hamiltonians of the delafossite proximate quantum spin liquid candidates KYbSe_2 and NaYbSe_2 , *Phys. Rev. B* **109**, 014425 (2024).
- [20] T. Treu, M. Klinger, N. Oefele, P. Telang, A. Jesche, and P. Gegenwart, Utilizing frustration in Gd- and Yb-based oxides for milli-Kelvin adiabatic demagnetization refrigeration, *J. Phys.: Condens. Matter* **37**, 013001 (2024).
- [21] Y. Tokiwa, S. Bachus, K. Kavita, A. Jesche, A. A. Tsirlin, and P. Gegenwart, Frustrated magnet for adiabatic demagnetization cooling to milli-kelvin temperatures, *Commun. Mater.* **2**, 42 (2021).
- [22] A. Jesche, N. Winterhalter-Stocker, F. Hirschberger, A. Bellon, S. Bachus, Y. Tokiwa, A. A. Tsirlin, and P. Gegenwart, Adiabatic demagnetization cooling well below the magnetic ordering temperature in the triangular antiferromagnet $\text{KBaGd}(\text{BO}_3)_2$, *Phys. Rev. B* **107**, 104402 (2023).
- [23] J. Xiang, C. Su, N. Xi, Z. Fu, Z. Chen, H. Jin, Z. Chen, Z.-J. Mo, Y. Qi, J. Shen, L. Zhang, W. Jin, W. Li, P. Sun, and G. Su, Dipolar Spin Liquid Ending with Quantum Critical Point in a Gd-based Triangular Magnet, [arXiv:2301.03571 \[cond-mat.str-el\]](https://arxiv.org/abs/2301.03571).
- [24] A. B. Kuznetsov, K. A. Kokh, N. Sagatov, P. N. Gavryushkin, M. S. Molokeev, V. A. Svetlichnyi, I. N. Lapin, N. G. Kononova, V. S. Shevchenko, A. Bolatov, B. Uralbekov, A. A. Goreiavcheva, and A. E. Kokh, Synthesis and Growth of Rare Earth Borates $\text{NaSrR}(\text{BO}_3)_2$ ($R = \text{Ho-Lu}, \text{Y}, \text{Sc}$), *Inorg. Chem.* **61**, 7497 (2022).
- [25] P. Dabić, V. Kahlenberg, B. Krüger, M. Rodić, S. Kovač, J. Blanuša, Z. Jagličić, L. Karanović, V. Petriček, and A. Kremenović, Low-temperature phase transition and magnetic properties of $\text{K}_3\text{YbSi}_2\text{O}_7$, *Acta Crystallogr. B* **77**, 584 (2021).
- [26] J. Rodríguez-Carvajal, Recent advances in magnetic structure determination by neutron powder diffraction, *Physica B Condens. Matter* **192**, 55 (1993).
- [27] See Supplemental Material at [http: LINK](http://LINK) for additional information.
- [28] A. Scheie, *PyCrystalField*: software for calculation, analysis and fitting of crystal electric field Hamiltonians, *J. Appl. Cryst.* **54**, 356 (2021).
- [29] R. M. Moon, W. C. Koehler, H. R. Child, and L. J. Raubenheimer, Magnetic Structures of Er_2O_3 and Yb_2O_3 , *Phys. Rev.* **176**, 722 (1968).
- [30] U. Arjun, K. M. Ranjith, A. Jesche, F. Hirschberger, D. D. Sarma, and P. Gegenwart, Adiabatic demagnetization refrigeration to millikelvin temperatures with the distorted square lattice magnet NaYbGeO_4 , *Phys. Rev. B* **108**, 224415 (2023).
- [31] S. Guchhait, A. Painganoor, S. S. Islam, J. Sichelschmidt, M. D. Le, N. B. Christensen, and R. Nath, Magnetic and crystal electric field studies of the rare earth based square lattice antiferromagnet NdKNaNbO_5 , *Phys. Rev. B* **110**, 144434 (2024).
- [32] K. Somesh, S. S. Islam, S. Mohanty, G. Simutis, Z. Guguchia, C. Wang, J. Sichelschmidt, M. Baenitz, and R. Nath, Absence of magnetic order and emergence of unconventional fluctuations in the $J_{\text{eff}} = \frac{1}{2}$ triangular-lattice antiferromagnet YbBO_3 , *Phys. Rev. B* **107**, 064421 (2023).
- [33] K. M. Ranjith, K. Brinda, U. Arjun, N. G. Hegde, and R. Nath, Double phase transition in the triangular antiferromagnet $\text{Ba}_3\text{CoTa}_2\text{O}_9$, *J. Phys.: Condens. Matter* **29**, 115804 (2017).
- [34] K. M. Ranjith, D. Dmytriieva, S. Khim, J. Sichelschmidt, S. Luther, D. Ehlers, H. Yasuoka, J. Wosnitza, A. A. Tsirlin, H. Kühne, and M. Baenitz, Field-induced instability of the quantum spin liquid ground state in the $J_{\text{eff}} = \frac{1}{2}$ triangular-lattice compound NaYbO_2 , *Phys. Rev. B* **99**, 180401 (2019).
- [35] K. M. Ranjith, S. Luther, T. Reimann, B. Schmidt, P. Schlender, J. Sichelschmidt, H. Yasuoka, A. M. Strydom, Y. Skourski, J. Wosnitza, H. Kühne, T. Doert, and M. Baenitz, Anisotropic field-induced ordering in the triangular-lattice quantum spin liquid NaYbSe_2 , *Phys. Rev. B* **100**, 224417 (2019).
- [36] S. Mugiraneza and A. M. Hallas, Tutorial: a beginner's guide to interpreting magnetic susceptibility data with the Curie-Weiss law, *Commun. Phys.* **5**, 95 (2022).

- [37] U. Arjun, K. Ranjith, A. Jesche, F. Hirschberger, D. Sarma, and P. Gegenwart, Efficient Adiabatic Demagnetization Refrigeration to below 50 mK with Ultrahigh-Vacuum-Compatible Ytterbium Diphosphates AYbP_2O_7 ($A=\text{Na, K}$), *Phys. Rev. Appl.* **20**, 014013 (2023).
- [38] M. Pula, S. Sharma, J. Gautreau, S. K. P., A. Kanigel, M. D. Frontzek, T. N. Dolling, L. Clark, S. Dunsiger, A. Ghara, and G. M. Luke, Candidate for a quantum spin liquid ground state in the Shastry-Sutherland lattice material $\text{Yb}_2\text{Be}_2\text{GeO}_7$, *Phys. Rev. B* **110**, 014412 (2024).
- [39] Y. Li, G. Chen, W. Tong, L. Pi, J. Liu, Z. Yang, X. Wang, and Q. Zhang, Rare-Earth Triangular Lattice Spin Liquid: A Single-Crystal Study of YbMgGaO_4 , *Phys. Rev. Lett.* **115**, 167203 (2015).
- [40] S. Thamban, U. Arjun, M. Padmanabhan, and R. Nath, Structural and magnetic properties of spin-1/2 dimer compound $\text{Cu}_2(\text{IPA})_2(\text{DMF})(\text{H}_2\text{O})$ with a large spin gap, *J. Phys.: Cond. Mat.* **29**, 255801 (2017).
- [41] P. Biswal, S. Guchhait, S. Ghosh, S. N. Sarangi, D. Samal, D. Swain, M. Kumar, and R. Nath, Crystal structure and magnetic properties of the spin- $\frac{1}{2}$ frustrated two-leg ladder compounds $(\text{C}_4\text{H}_{14}\text{N}_2)\text{Cu}_2\text{X}_6$ ($X = \text{Cl, Br}$), *Phys. Rev. B* **108**, 134420 (2023).
- [42] C. Kittel, *Introduction to Solid State Physics*, 8th ed. (John Wiley & Sons, Inc., New York, 1986).
- [43] R. Nath, M. Padmanabhan, S. Baby, A. Thirumugan, D. Ehlers, M. Hemmida, H.-A. Krug von Nidda, and A. A. Tsirlin, Quasi-two-dimensional $S = \frac{1}{2}$ magnetism of $\text{Cu}[\text{C}_6\text{H}_2(\text{COO})_4][\text{C}_2\text{H}_5\text{NH}_3]_2$, *Phys. Rev. B* **91**, 054409 (2015).
- [44] S. Guo, A. Ghasemi, C. L. Broholm, and R. J. Cava, Magnetism on ideal triangular lattices in $\text{NaBaYb}(\text{BO}_3)_2$, *Phys. Rev. Mater.* **3**, 094404 (2019).
- [45] D. J. Newman and B. Ng, *Crystal Field Handbook* (Cambridge University Press, 2000).
- [46] K. W. H. Stevens, Matrix elements and operator equivalents connected with the magnetic properties of rare earth ions, *Proc. Phys. Soc. Section A* **65**, 209 (1952).
- [47] M. Hutchings, *Point-Charge Calculations of Energy Levels of Magnets*, Solid State Physics, Vol. 16 (Academic Press, 1964) p. 227.
- [48] S. Mohanty, S. S. Islam, N. Winterhalter-Stocker, A. Jesche, G. Simutis, C. Wang, Z. Guguchia, J. Sichelschmidt, M. Baenitz, A. A. Tsirlin, P. Gegenwart, and R. Nath, Disordered ground state in the spin-orbit coupled $J_{\text{eff}} = \frac{1}{2}$ distorted honeycomb magnet BiYbGeO_5 , *Phys. Rev. B* **108**, 134408 (2023).
- [49] H. J. Xiang, E. J. Kan, S.-H. Wei, M.-H. Whangbo, and X. G. Gong, Predicting the spin-lattice order of frustrated systems from first principles, *Phys. Rev. B* **84**, 224429 (2011).
- [50] S. J. Sebastian, S. S. Islam, A. Jain, S. M. Yusuf, M. Uhlarz, and R. Nath, Collinear order in the spin- $\frac{5}{2}$ triangular-lattice antiferromagnet $\text{Na}_3\text{Fe}(\text{PO}_4)_2$, *Phys. Rev. B* **105**, 104425 (2022).